Journal of Solar Energy Research (JSER)

Journal homepage: www.jser.ut.ac.ir

One-Year Assessment of Passive Cooling Options for Photovoltaic Modules in Hot-Arid Conditions Using Field-Calibrated Data and Simulation

Yousef Adel Altaharwah

Department of Mechanical Engineering, Faculty of Engineering, Mutah University, Al-Karak 61710, Jordan

ARTICLE INFO

Article Type:

Research Article

Received:2026.07.23
Accepted in revised form:2026.11.27

Keywords:
Cost ceiling; Heat-loss coefficient; Optical penalty; Rear fins; Thermal screening; Uncertainty propagation

A B S T R A C T

Improving photovoltaic (PV) performance through passive cooling offers a potential approach to increasing electricity generation under hot-arid conditions. This study assessed rear fins, enhanced emissivity, and their combination using 2020 data from the Sandia National Laboratories/PV Performance Modeling Collaborative (PVPMC) datasets for Albuquerque. The analysis included 527,041 one-minute temperature records, monthly Faiman–radiation coefficients, and 3,994 daylight hours. Field measurements were available only for the reference module, while the cooling configurations were evaluated numerically under identical annual meteorological conditions. Therefore, the reported improvements represent model-based screening estimates rather than experimentally validated cooling performance. Rear fins were predicted to reduce mean daylight module temperature by 2.54 °C, decrease operating hours above 55 °C from 437 to 158 h, and increase normalized annual DC yield by 34.20 kWh kWp^{-1} (1.56%). Enhanced emissivity produced an ideal modeled gain of 0.061%, offset at a break-even solar-band optical loss of 0.068%. The ideal hybrid configuration achieved a 1.61% gain, providing only 1.10 kWh kWp^{-1} more than fins alone. Across 3,000 Latin hypercube samples, positive gains were predicted for 100.0% of fin cases, 6.1% of radiative cases, and 99.9% of hybrid cases.

1. Introduction

In outdoor installations, photovoltaic (PV) modules act as both energy converters and thermal interfaces with their surroundings, as discussed by Jones and Underwood [1]. Although 25 °C is the standard reference cell temperature, actual operating temperatures vary under field conditions [2]. Module temperature depends on incident irradiance and convective and radiative heat losses, as described by Faiman [3]. The effects of temperature and wind speed on PV performance have been investigated

* Corresponding author Email: y.altaharwah@mutah.edu.jo

Cite this article: Altaharwah, Y. A. (2026). One-Year Assessment of Passive Cooling Options for Photovoltaic Modules in Hot-Arid Conditions Using Field-Calibrated Data and Simulation. Journal of Solar Energy Research, 11(4), 3452–3465. https://doi.org/10.22059/jser.2026.419153.1773

DOI: 10.22059/jser.2026.419153.1773

©The Author(s). Publisher: University of Tehran Press.

experimentally by Kaldellis et al. [4] and under practical operating conditions by Du et al. [5]. Skoplaki and Palyvos [6] comprehensively reviewed the temperature dependence of PV electrical performance.

High thermal loading can occur under strong solar irradiance, high ambient temperatures, clear skies, and limited heat dissipation. Rear-side convection depends on mounting configuration and wind conditions, whereas long-wave radiative exchange depends on sky conditions and view factor. Convective heat loss is represented in Faiman's model [3], while Driesse et al. [7] analysed the role of long-wave radiation.

Under such conditions in cities, the performance of photovoltaics (PVs) could be further impacted by the urban heat island (UHI) phenomenon, which creates local heating above those observed in non-urban locations. According to Han et al. [8], the effects of UHI could lower the efficiency of PV conversions in densely developed areas. In a similar manner, Golzarroshan et al. [9] found that an average of 2.01 °C increase in temperature due to UHI effects in Mashhad, Iran, has led to an annual decrease in PV power production in residential buildings by 162.4 kWh.

There are extra considerations regarding the thermal performance of BIPV since the heat removal process relies on the building configuration. In their study about energy performance of façade integrated PV system in an office building in Tehran, Hoseinzadeh et al. [10] have discussed the relevance of BIPV to the building energy performance. Talaei and Sangin [11], on the other hand, conducted a more recent study on the effects of different types of BIPV in desert, steppe, and Mediterranean climates.

PV cooling systems can be divided into two major categories: active and passive. Active cooling includes forced air cooling, water cooling, spray cooling, and evaporative cooling. The use of forced air cooling in order to increase PV efficiency was studied by Mustafa et al. [12]. Passive cooling, on the other hand, requires minimal to zero external power, and thus it is considered to be a good method for PV thermal control [13, 14].

Rear fins are among the passive cooling options considered in this study. By increasing the rear surface area, they enhance convective heat dissipation from the PV module. Bayrak et al. [15] examined the effects of fin geometry on module temperature and efficiency. Hernandez-Perez et al. [16] investigated passive PV heat sinks through numerical and experimental analyses and subsequently studied discontinuous fin configurations [17]. Dida et al. [18] experimentally evaluated passive cooling under hot-arid conditions. These studies indicate that cooling performance depends strongly on fin dimensions, spacing, orientation, thermal conductivity, mounting conditions, and airflow. Consequently, findings for a particular fin arrangement cannot be directly generalized to other installations. An important consideration is whether the expected annual energy gain can justify the additional installation and maintenance costs.

Another form of passive cooling that was studied is radiative cooling. This was done by Raman et al. [19], who showed the viability of radiative cooling as a means of rejecting heat below ambient temperature. Another researcher who looked at radiative cooling technology is Zhu et al. [20], who applied it to solar cells. Safi and Munday [21] analyzed the possibility of improving photovoltaic performance through radiative cooling, while Sun et al. [22] explored selective spectral techniques for PV cooling applications. Although radiative cooling has a mechanically simple design, it needs a very high optical transparency in the useful solar spectrum.

Publicly available PV datasets enable annual thermal assessments using measured environmental conditions. Data related to PV module performance and resource weather from Theristis & Stein [23] was used as meteorological input data in this study. Temperature data for reference modules was collected using database prepared by Driesse et al. [24] and detailed in their report [25].

The field measurements were limited to the reference PV module, with no experimental data available for the finned, coated, or hybrid configurations. Accordingly, the measured data were used to calibrate the baseline thermal model, while the cooling configurations were evaluated numerically. Therefore, the predicted cooling performance should not be interpreted as experimental validation of the proposed cooling strategies.

This study aimed to establish a monthly thermal baseline using 2020 PV module temperature measurements and evaluate rear-fin, enhanced-emissivity, and hybrid cooling configurations under the corresponding hourly weather conditions. The assessment considered temperature reduction, high-temperature exposure, changes in normalized direct current (DC) energy yield, optical-loss tolerance, uncertainty intervals, and economic constraints. These results provide a preliminary ranking of passive cooling options to guide the selection of

configurations for future year-long, side-by-side experimental testing.

2. Materials and Methods

The analysis used two annual datasets (Fig. 1 and Table 1). The first provided reference-module temperature measurements and monthly Faiman–radiation coefficients, while the second supplied hourly meteorological data for energy-yield, thermal-exposure, uncertainty, and economic assessments. Reference-module temperatures were obtained from the Sandia/PVPMC resources [24, 25], and the corresponding weather data from the PVPMC dataset [23]. All configurations were evaluated using the same accepted weather hours. Four cases were considered: C_0 represents the reference module, C_1 includes rear fins, C_2 assumes enhanced emissivity, and C3 combines both cooling approaches. The ideal deterministic C_2 and C_3 cases assume zero solar-band optical loss, while optical loss is varied in the sensitivity and uncertainty analyses.

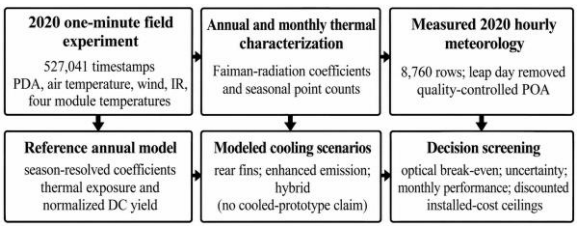


Figure 1. Annual data and calculation workflow used to screen the modeled cooling cases

Table 1. Data sources and analytical roles used in the annual screening workflow

Source	Time basis	Inputs	Role
PV temperature data	2020, 1-min	POA irradiance; T_a; v; sky IR; four back-temperature	Monthly fits
Measured weather year	2020, hourly	GHI; DNI; DHI; T_a; RH;	Annual forcing
Cooling designs	Modeled cases	Fin geometry; emissivity; optical loss	Scenario screening

Abbreviations: POA, plane-of-array; GHI, global horizontal irradiance; DNI, direct normal irradiance; DHI, diffuse horizontal irradiance; RH, relative humidity; IR, infrared.

The reference data were obtained from the Sandia National Laboratories/PV Performance Modeling Collaborative (PVPMC) module-temperature dataset provided by Driesse et al. [24] and documented in [25]. The Albuquerque dataset contains 527,041 one-minute records from south-facing modules tilted at 35°, including tilted irradiance, ambient conditions, wind speed, infrared sky exchange, and four rear-temperature sensor readings. The reference module was a 325 W Panasonic heterojunction with intrinsic thin layer (HIT) module featuring 96 cells, an area of 1.67427 m², 19.41% nominal efficiency, and a power-temperature coefficient of −0.0042 K^{-1}. Data processing involved averaging the two upper rear-temperature sensor readings, applying a 25-minute moving average, and fitting the radiation-augmented Faiman model described by Driesse et al. [7, 25].

The source documentation reports a data gap in January, preceded by an inverter shutdown. Accordingly, the 2020 dataset was treated as a calendar-year baseline comprising eleven complete months and a partial January. Table 2 lists the monthly fitting counts. Initial daytime screening retained 249,587 observations; after applying a 25-minute moving average and removing incomplete windows, 240,539 observations were used for monthly fitting, ranging from 11,499 to 24,302 per month.

Table 2. Monthly Faiman-radiation coefficients fitted from the 2020 one-minute temperature record

Calendar month	U_0 (W m^{-2} K^{-1})	U_1 (W m^{-2} K^{-1} per m s^{-1})	Fitted daylight points
1	20.33	5.75	11,499
2	21.45	5.44	17,230
3	21.68	4.88	20,599
4	21.57	4.66	21,994
5	21.99	3.83	24,258
6	22.71	3.72	23,581
7	23.37	3.91	24,302
8	24.06	3.55	22,794
9	22.61	4.68	20,686
10	23.13	4.24	19,483

11	21.95	5.23	17,252
12	21.70	6.24	16,861

Hourly meteorological data were obtained from the PVPMC performance dataset described by Theristis and Stein [23]. Excluding leap day yielded 8,760 hourly records for 2020. The variables included GHI, DNI, DHI, dry-bulb temperature, relative humidity, and wind speed. Since hourly averages were timestamped at the end of each hour, timestamps were shifted backward by 30 minutes. Irradiance on the fixed south-facing tilted plane was calculated using the Perez transposition model implemented in pvlib-python [26, 27], assuming an albedo of 0.20. After screening for physically plausible weather conditions and retaining hours with plane-of-array (POA) irradiance above 50 W m^{-2}, 3,994 daylight hours remained. The screening limits are listed in Table 3.

Hourly downwelling long-wave irradiance was unavailable in the weather dataset and was therefore estimated from ambient temperature using Swinbank's clear-sky formulation [28]. The model was applied to all retained hours without cloud-state filtering, although the dataset may include clear, partly cloudy, and cloudy conditions. Since clouds generally increase downwelling long-wave radiation relative to clear skies, this approach may introduce bias. Its influence on the annual results was assessed through a systematic sensitivity analysis, applying biases ranging from −100 to +100 W m^{-2} to the estimated irradiance.

Table 3. Quality-control limits used for the annual weather file

Screened quantity	Permitted values
GHI	>0 and <1,300 W m^{-2}
DNI	≥0 and <1,200 W m^{-2}
DHI	≥0 and <800 W m^{-2}
Wind speed	>0 and <32 m s^{-1}
Relative humidity	>0 and <100%
Ambient temperature	-5 to 45 °C
Plane-of-array irradiance	>50 W m^{-2} for annual metrics

Module temperature was estimated using the Faiman heat-balance formulation [3], incorporating long-wave radiative exchange with the sky following Driesse et al. [7], as expressed in Eq. (1). The monthly U_0 values ranged from 20.33 to 24.06 W m^{-2} K^{-1}, while U_1 ranged from 3.55 to 6.24 W m^{-2} K^{-1} per m s^{-1}. The annual coefficients (U_0 = 22.72 and U_1 = 4.35) were used only for comparison.

$$T_m = T_a + \frac{G - \varepsilon F_{sky}[\sigma(T_a + 273.15)^4 - L\downarrow]}{U_{0,m} + U_{1,m}\upsilon + U_{fin}} \quad (1)$$

where T_m and T_a denote module and ambient temperatures, respectively; G is plane-of-array irradiance; ε is emissivity; F_{sky} is the sky-view factor; σ is the Stefan–Boltzmann constant; $L_\downarrow$ is downwelling long-wave irradiance; υ is wind speed; $U_{0,m}$ and $U_{1,m}$ are monthly heat-loss coefficients; and U_{fin} represents additional fin conductance. The fitted coefficients combine several heat-transfer effects, including convection, radiation, and thermal storage, which cannot be independently resolved through the Faiman model. Consequently, these coefficients are specific to the reference module, its mounting configuration, and site conditions, and should not be directly applied elsewhere. The modeled cooling contributions are evaluated relative to this baseline and should not be interpreted as independently fitted empirical coefficients.

The robustness of the reference formulation was assessed using fitting diagnostics from the Sandia/PVPMC temperature dataset. Initial daytime screening retained 249,587 observations; after applying the 25-minute moving average and removing incomplete windows, 240,539 observations remained for monthly Faiman–radiation fitting. The fitted U_0 values ranged from 20.33 to 24.06 W m^{-2} K^{-1}, while U_1 ranged from 3.55 to 6.24 W m^{-2} K^{-1} per m s^{-1}, indicating seasonal variation. The full processed record yielded U_0 = 22.72 W m^{-2} K^{-1} and U_1 = 4.35 W m^{-2} K^{-1} per m s^{-1}. Restricting the fit to G > 800 W m^{-2} retained 81,689 observations and yielded U_0 = 22.18 W m^{-2} K^{-1} and U_1 = 4.34 W m^{-2} K^{-1} per m s^{-1}, representing changes of approximately −2.4% and −0.2%, respectively. These small differences support the stability of the fitted relationship under high irradiance. However, larger changes under high module-to-ambient temperature differences indicate that the coefficients vary across thermal regimes, supporting the use of month-specific values.

Driesse et al. [7] evaluated the radiation-augmented Faiman model using one year of measurements from the same Sandia field campaign. Including long-wave radiative losses reduced the daytime mean bias error (MBE) from 0.85 to −0.03 °C and the root mean square error (RMSE) from 2.43 to 1.68 °C compared with the conventional Faiman model. These results support the selected

model formulation but do not represent validation statistics for the month-specific coefficients used in this study. Furthermore, independent validation errors under low-wind, high-wind, and high-ambient-temperature conditions were not determined for the present parameterization. Therefore, model performance under these specific conditions remains unverified.

For C_1, an additional convective term was introduced in the denominator of Eq. (1). The nominal modeled heat sink had an added fin-area ratio of 1.0, aluminum thermal conductivity of 205 W m^{-1} K^{-1}, fin length of 50 mm, thickness of 1.5 mm, and contact effectiveness of 0.90. These values represent engineering assumptions for preliminary screening rather than measured properties of an installed finned module. The selection of rear-fin cooling was guided by previous PV heat-sink studies [15-17]. The fin conductance and straight-fin models in Eqs. (2)–(5) follow conventional fin theory, informed by these studies. The additional fin conductance was calculated using Eq. (2):

$$U_{\text{fin}} = \eta_c \eta_f h (A_f / A_p) \quad (2)$$

where η_c is the fin-to-module contact effectiveness, η_f is the fin efficiency, h is the convective heat-transfer coefficient, and A_f/A_p is the added fin-area ratio. The straight-fin efficiency was calculated using Eq. (3):

$$\eta_f = \tanh(mL_c) / (mL_c) \quad (3)$$

The fin parameter m was calculated from Eq. (4):

$$m = [2h / (kt)]^{1/2} \quad (4)$$

The corrected fin length was determined using Eq. (5):

$$L_c = L + t/2 \quad (5)$$

This corresponds to the conventional corrected-length approximation used for PV fin analysis by Bayrak et al. [15]. The fin-surface convective heat transfer coefficient was represented by the reduced-order relation in Eq. (6):

$$h = h_0 + h_v \upsilon \quad (6)$$

where h_0 = 3 W m^{-2} K^{-1} and h_υ = 2 W m^{-2} K^{-1} per m s^{-1} are the nominal coefficients. Equation (6) has the same structure as that of the wind dependent convective correlation used by Palyvos [29], but with coefficients varying with the geometry of the surface, orientation and exposure to winds. These values were taken for the initial analysis of the suggested fins arrangement, without having been experimentally validated. The modeling uses fins with an equivalent increased surface area, without explicitly considering the effects of fin spacing, wind orientation, channel obstruction and 3D wakes.

As for C_2, the long-wave emissivity of the surface is increased from 0.88 to 0.95 as a result of the previous experience with radiative cooling surfaces [19-22]. The value has not been measured for the real coating. The initial deterministic analysis assumes zero optical loss in the solar band to find the maximum cooling effect. C_3 is a combination of the rear fins and enhanced emissivity. The baseline values of U_0 and U_1 were kept the same in all configurations for the analysis of the cooling effect only.

DC power per hour was normalized on peak capacity. Fractional loss of light intensity, ℓ, affects irradiance prior to the electricity calculations. Cell temperature is calculated from module back temperature using irradiance-dependent value of 3 °C at 1,000 W m^{-2}. Normalized DC power was calculated using Eq. (7) with $\gamma = -0.0042$ K^{-1} as per Dobos [30]. Negative power values were set to zero. Inverter efficiency, clipping, wiring losses, module mismatch, soiling, system availability, degradation, and additional spectral effects were excluded to isolate the modeled cooling contributions.

$$\frac{P_{\text{DC}}}{P_{\text{STC}}} = [(1-\ell)G/1000] \times [1+\gamma(T_c - 25)] \quad (7)$$

where P_{DC} is the DC output power, P_{STC} is the rated power at standard test conditions (1,000 W m^{-2} and 25 °C), ℓ is the solar-band optical-loss fraction, G is the plane-of-array irradiance, γ is the power-temperature coefficient (−0.0042 K^{-1}), and T_c is the cell temperature. Thermal outputs include mean, irradiance-weighted, 95th-percentile, and maximum module temperatures; mean and 95th-percentile cooling; and operating hours above 45, 55, and 65 °C. Electrical outputs include annual normalized DC yield, absolute and percentage yield gains relative to C_0, and monthly gains. For C_2 and C_3, ℓ was varied from 0 to 2.0% in 0.05% increments, with temperature and power recalculated at each step to account for reduced solar absorption. Break-even optical loss was determined by interpolation where annual yield gain relative to C_0 changed sign. Uncertainty was assessed using 3,000 Latin hypercube samples (LHS), following McKay et al. [31], with a fixed random seed of 20260622. Uncertain inputs included heat-loss coefficients, fin and coating properties, module temperature sensitivity, and convection parameters. The U_0 and U_1 multipliers followed bounded normal distributions, while other parameters used uniform ranges. All parameters were sampled independently, as summarized in Table 4.

The parameter ranges in Table 4 were selected as engineering screening values rather than statistically

derived from experimental observations. The thermal, fin-convection, and electrical models were adopted from previous studies [3, 7, 15, 29, 30]. Uncertainties in the long wave radiation have been determined independently in a bias test of −100 to +100 W m^{-2}, instead of considering them in the probabilistic LHS approach. For every sampled data set, C_0 was calculated based on the sampled thermal and electrical parameters before any cooling variations. The use of both sets in combination eliminates the confusion between uncertainty in the parameters and cooling effects. The uncertainty ranges presented in the results are those of the 2.5th, median, and 97.5th percentile of the output of the model. The sufficiency of the sample size was checked using 1,000, 2,000, and 3,000 Latin Hypercube sampling with the same input distribution and fixed random seed.

Table 4. Input distributions used in the Latin hypercube uncertainty analysis

Parameter	Dist.	Min.	Max.	Center	SD
U_0 multiplier	N	0.85	1.15	1.00	0.05*
U_1 multiplier	N	0.70	1.30	1.00	0.10*
A_f/A_p	U	0.60	1.40	1.00	0.231
η_c	U	0.70	1.00	0.85	0.087
ε	U	0.90	0.97	0.935	0.020
ℓ	U	0	0.80%	0.40%	0.231%
γ (10^{-3} K^{-1})	U	−4.5	−3.5	−4.0	0.289
h_0	U	2.0	5.0	3.5	0.866
h_v	U	1.0	3.0	2.0	0.577

* N: clipped normal distribution; U: uniform distribution. The standard deviations reported for U_0 and U_1 correspond to the underlying normal distributions before clipping.

Because installation cost information of the proposed cooling system arrangements was not available, their annual energy gains were transformed into maximum economical cost values per kWp. Monetary units are given in USD, while the exchange rate used is 1 Jordanian dinar (JOD) = 1.41046 USD. Three electricity prices (0.071, 0.141, and 0.212 USD/kWh) and three economical time frames (3, 5, and 10 years) have been used as sample cases instead of any verified tariffs or project-specific parameters. In all proposed cooling configurations, a discount rate of 6% and a yearly PV energy degradation rate of 0.5% have been considered. The discount rate is in accordance with the NREL Q1 2020 PV Cost Benchmark published by Feldman et al. [32], where it was estimated that the real equity discount rates are 6.1% for residential and commercial PV and 5.1% for utility-scale PV. The energy degradation rate of 0.5% per year has been considered due to the findings reported by Jordan and Kurtz [33], where the median value of nearly 2,000 observations has been approximately 0.5%. For all cooling configuration systems, the degradation rate has been considered because the dependency of the cooling on degradation has not been validated. Also, reliability improvements, coating degradation, and price escalation have been assumed as constant because the change of coating and monetary values have not been taken into consideration.

$$C_{\max} = \sum_{y=1}^{N} \frac{\Delta E_1 (1-d)^{y-1} P_e}{(1+r)^y} \quad (8)$$

where C_{max} is the maximum allowable installed cost (USD kWp^{-1}), ΔE_1 is the first-year incremental energy yield (kWh kWp^{-1}), P_e is the electricity price (USD kWh^{-1}), d is the annual degradation rate, r is the real discount rate, and N is the analysis period (years). Equation (8) applies discounted present-value analysis, with the discount and degradation rates based on Feldman et al. [32] and Jordan and Kurtz [33], respectively.

3. Results and Discussion

After excluding leap day, the 2020 weather dataset contained 8,760 hourly records. Applying meteorological screening criteria and the plane-of-array irradiance threshold yielded 3,994 daylight hours. February had the fewest retained hours (275 h), while July had the most (373 h).

Table 5 summarizes the retained weather data. Monthly plane-of-array (POA) irradiation ranged from 152.25 kWh m^{-2} in February to 229.86 kWh m^{-2} in May (Fig. 2). Mean daylight ambient temperature ranged from 5.17 °C in January to 31.23 °C in August, while mean wind speed varied between 2.87 and 4.06 m s^{-1}. These variations reflect seasonal changes in solar resources and

thermal conditions. Retaining hourly irradiance, temperature, and wind-speed records preserves their simultaneous variation and avoids the bias associated with considering only hot or mild periods. This approach provides a more representative assessment of annual cooling requirements, high-temperature exposure, and modeled peak module temperatures.

Table 5. Monthly accepted hours and resource conditions after screening

Month	Retained hours	POA irradiation (kWh m^{-2})	Average T_a (°C)	Average v (m s^{-1})
1	288	163.05	5.17	3.18
2	275	152.25	8.90	3.88
3	335	189.69	14.73	3.98
4	355	221.39	19.02	4.06
5	370	229.86	25.58	3.97
6	360	213.28	29.42	3.87
7	373	206.71	30.70	3.12
8	366	212.14	31.23	2.87
9	352	214.03	25.01	3.51
10	334	213.99	20.12	3.18
11	291	173.96	13.91	3.50
12	295	174.41	5.76	3.16

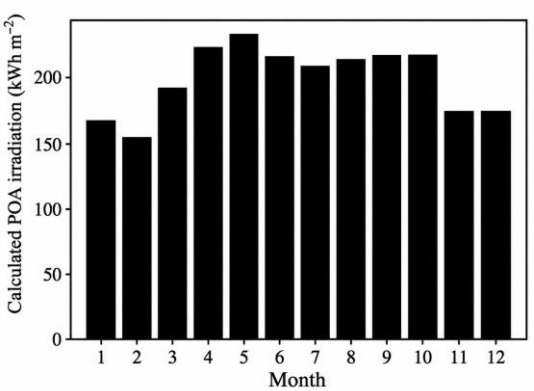


Figure 2. Monthly plane-of-array (POA) irradiation calculated from the screened 2020 hourly weather data

The sensitivity of the annual results to the plane-of-array (POA) irradiance threshold was examined using values of 0, 25, 50, and 100 W m^{-2}. Reducing the threshold from 50 to 0 W m^{-2} increased the retained hours from 3,994 to 4,704 and the reference normalized yield from 2,186.95 to 2,196.96 kWh kWp^{-1}, a difference of only 0.46%. Mean reference-module temperature decreased from 34.58 to 31.99 °C because the additional hours involved cooler, low-irradiance conditions. However, cooling gains remained nearly unchanged. Fin, radiative, and hybrid gains shifted from 1.564%, 0.061%, and 1.614% at 50 W m^{-2} to 1.556%, 0.061%, and 1.607% at 0 W m^{-2}, respectively.

The ranking of cooling options remained unchanged across all tested irradiance thresholds. The fitted heat-loss coefficients showed clear seasonal variation (Fig. 3). U_0 increased from 20.33 W m^{-2} K^{-1} in January to 24.06 W m^{-2} K^{-1} in August before declining toward winter. In contrast, U_1 reached its maximum in December (6.24), remained relatively high in January (5.75), and decreased to its minimum in August (3.55), with values expressed in W m^{-2} K^{-1} per m s^{-1}. Using monthly rather than annual heat-loss coefficients reduced the mean modeled reference-module temperature from 34.639 to 34.576 °C and increased normalized annual DC yield from 2,186.04 to 2,186.95 kWh kWp^{-1} (Table 6). The yield difference was 0.91 kWh kWp^{-1}, while the 95th-percentile module temperature increased from 58.511 to 59.060 °C.

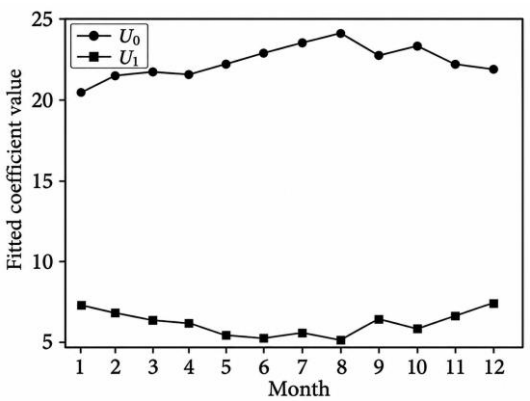


Figure 3. Monthly variation in fitted Faiman–radiation coefficients for the reference PV module in

2020. U_0 represents the zero-wind heat-loss coefficient (W m^{-2} K^{-1}), while U_1 represents the wind-dependent heat-loss coefficient (W m^{-2} K^{-1} per m s^{-1})

Table 6. Sensitivity to monthly versus annual reference coefficients

Coefficient set	Mean T_m (°C)	P95 T_m (°C)	Normalized yield (kWh kWp^{-1})
Monthly	34.576	59.060	2186.95
Annual	34.639	58.511	2186.04

For the reference case C_0, mean daylight module temperature was 34.58 °C, with an irradiance-weighted mean of 40.57 °C, a 95th-percentile temperature of 59.06 °C, and a maximum of 68.48 °C. Operating hours above 45, 55, and 65 °C were 1,116, 437, and 11, respectively, indicating substantial high-temperature exposure despite the moderate mean temperature. The reference normalized annual DC yield was 2,186.95 kWh kWp^{-1}. This represents a comparative baseline rather than actual plant yield, as inverter and other system losses were excluded. All cooling configurations were evaluated using identical weather conditions and electrical assumptions (Table 7). Rear fins (C_1) increased normalized yield by 34.20 kWh kWp^{-1} (1.56%), with smaller annual gains than peak-temperature improvements might suggest because cooler periods contribute to annual production. Enhanced emissivity (C_2) reduced mean temperature by only 0.135 °C and increased yield by 1.33 kWh kWp^{-1} (0.061%). The ideal hybrid (C_3) reduced mean temperature by 2.65 °C and increased yield by 35.30 kWh kWp^{-1} (1.61%). Compared with fins alone, the hybrid provided an additional 0.112 °C temperature reduction and 1.10 kWh kWp^{-1} in normalized yield, indicating that the radiative contribution offers limited additional benefit unless optical losses and incremental costs are negligible.

Table 7. Deterministic annual thermal and normalized-yield results

Case	Mean T_m (°C)	P95 T_m (°C)	Time above 55 °C (h)	Yield (kWh kWp^{-1})	Gain (%)
C_0	34.58	59.06	437	2186.95	0.000
C_1	32.04	54.17	158	2221.15	1.564
C_2	34.44	58.94	426	2188.28	0.061
C_3	31.93	54.09	152	2222.25	1.614

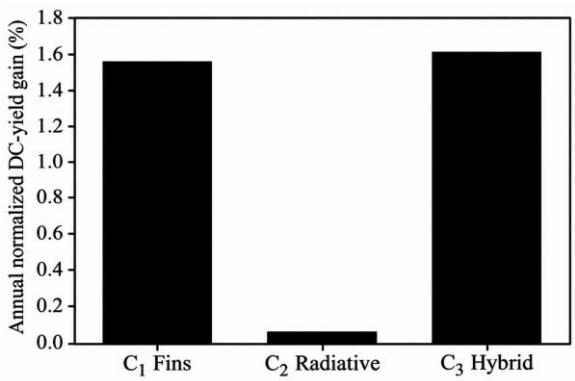


Figure 4. Annual normalized DC-yield gain for the modeled passive-cooling cases

C_1 and C_3 reduced mean module temperature throughout the year (Fig. 5). For C_1, monthly cooling ranged from 2.05 °C in February to 3.04 °C in May, while C_3 achieved reductions of 2.17–3.14 °C. In contrast, C_2 provided only minor cooling, ranging from 0.10 to 0.16 °C.

The high-temperature exposure results followed a similar trend. C_1 reduced operating time above 45 and 55 °C by 260 and 279 h, respectively, while C_3 achieved reductions of 269 and 285 h. C_2 showed only a limited improvement. For reliability-related assessments, reductions in prolonged high-temperature exposure are more informative than changes in mean energy yield

alone.

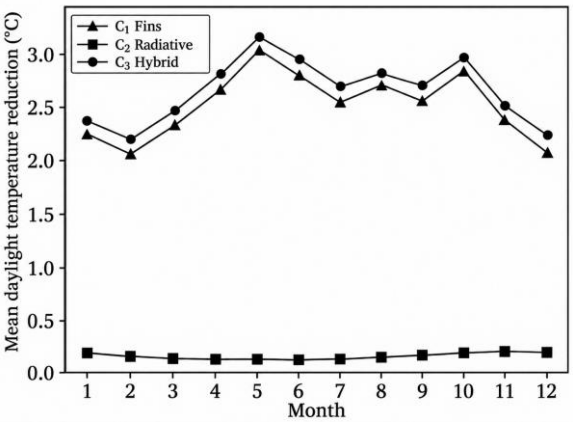


Figure 5. Monthly daylight cooling relative to the uncooled reference

C_2 was highly sensitive to solar-band optical losses (Table 8 and Fig. 6). Its ideal annual yield gain of 0.061% was eliminated at an optical loss of 0.068%. Thus, even a 0.1% reduction in usable solar irradiance would outweigh the cooling benefit. On the other hand, C_3 could sustain higher optical losses owing to the 1.56% benefit from the rear fins. The hybrid arrangement achieved an optical loss break-even point of 1.742% with respect to C_0. Nevertheless, this is applicable to the entire hybrid system rather than just the emissive layer. In order to beat the performance of fins alone, the emissive layer should retain almost all the extra 1.10 kWh kWp^{-1} benefit.

Soiling may influence the efficiency of the passive radiative cooling system in hot and arid areas due to changes in the optical properties of the surface. Huang et al. [34] examined the influence of the dust characteristics on the performance of the radiative-cooling PV systems, whereas Hossain et al. [35] gave an overview of the anti-soiling coatings in the deserts. In the case of C_2, the optimal modeled yearly gain in the yield of 0.061% disappeared for the solar band optical losses of 0.068%. Rear fin cooling is independent of the optical properties of the coating.

Table 8. Solar-band optical-loss limits for the radiative cases

Option	Zero-loss gain (%)	Break-even loss (%)	Extra yield over fins (kWh kWp^{-1})
Radiative only	0.061	0.068	Not applicable
Hybrid	1.614	1.742	1.10

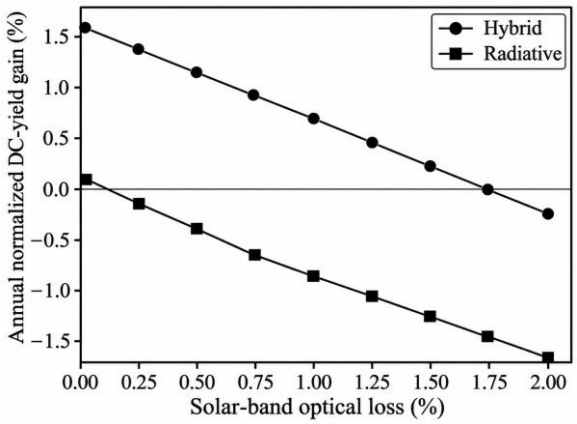


Figure 6. Annual normalized DC-yield gain versus solar-band optical loss

The uncertainty analysis changed the deterministic ranking, placing C_1 ahead of C_3 and C_2 (Table 9 and Fig. 7). C_1 achieved a median annual yield gain of 1.43%, with a 2.5th–97.5th percentile interval of 0.76–2.41% and positive gains in all 3,000 samples. C_3 showed a median gain of 1.11% (0.28–2.13%), with positive gains in 99.9% of samples. Under deterministic ideal conditions, C_3 beat C_1 by 0.05 percentage points; however, taking into account optical losses, the median predicted gain decreased. C_2 had a median gain of -0.31% with the 2.5th – 97.5th percentile interval of -0.66% to 0.03%. Only 6.1% of the samples provided positive results. This loss in energy yield was explained by optical losses and not the elevated temperatures of the modules. Despite the overlapping uncertainty intervals, C_1 had positive gains in all the samples. The performance of C_1 and C_3 was influenced by fin geometry, contact effectiveness, and convection, whereas optical losses affected the enhanced-emissivity configurations, C_2 and C_3. The uncertainty in the common heat loss coefficients had little effect on the predicted gain as every configuration was compared to the re-computed reference scenario. Sensitivity to long-wave irradiance estimation was considered separately using systematic biases

introduced into the clear-sky model proposed by Swinbank, which was used without cloud-filtering. Under biases between -100 and +100 W m^{-2}, the annual gain ranged from 1.39% to 1.75% in C_1 and from 1.50% to 1.73% in C_3. On the contrary, C_2 showed a drop from 0.135% under -100 W m-2 bias to -0.015% under +100 W m^{-2} bias with gain equaling zero at bias of +80.5 W m^{-2}. Thus, it can be stated that the benefit of rear fins proves to be robust under the given range of bias, while the small radiative-only gain turns out to be less robust to the uncertainty in long-wave radiation.

Table 9. Latin-hypercube annual yield-gain intervals

Case	Runs	P2.5 (%)	Median (%)	P97.5 (%)	Positive (%)
C_1	3000	0.76	1.43	2.41	100.0
C_2	3000	-0.66	-0.31	0.03	6.1
C_3	3000	0.28	1.11	2.13	99.9

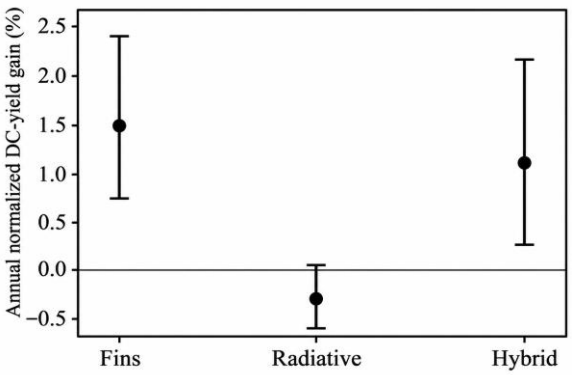


Figure 7. Median annual yield gain and 2.5th-97.5th percentile uncertainty intervals

The Latin hypercube results showed good stability across the tested sample sizes. Increasing the sample size from 2,000 to 3,000 changed the 2.5th, median, and 97.5th percentile estimates by at most 0.063 percentage points. The median ranking remained unchanged at all tested sample sizes, with C_1 (fins) followed by C_3 (hybrid) and C_2 (radiative). Accordingly, 3,000 samples were considered adequate for the present screening analysis.

In the context of the central economic case of 0.141 USD kWh^{-1} and a 10-year planning horizon, the upper bounds on the gross installed costs were 34.80 USD kWp^{-1} for C_1, 1.35 USD kWp^{-1} for ideal C_2, and 35.92 USD kWp^{-1} for ideal C_3 (Table 10 and Fig. 8). These figures were approximately reduced by half at 0.071 USD kWh^{-1}. The low upper bound for C_2 makes the radiative coating uneconomical unless it has a negligible cost or adds to reliability. The upper bound on the ideal hybrid exceeds that on the fin-only by 1.12 USD kWp^{-1} only, providing little economic room for adding the radiative coating. This result is consistent with the optical loss analysis showing that high transmissivity in the solar band and small costs are necessary for the effective radiative cooling. The above cost ceilings are meant for preliminary economic evaluation and do not reflect real installation costs. The practical application will necessitate consideration of electricity prices, financing conditions, possible changes in construction, wind loading, installation costs, warranty and maintenance, and end-of-life disposal.

The economic assessment does not account for possible financial benefits associated with slower PV module degradation or longer service life due to reduced operating temperatures. While the modeled C_1 and C_3 configurations considerably decreased exposure to high temperatures, their effects on long-term degradation and failure risk could not be reliably estimated because sufficient lifetime data were unavailable. Therefore, the energy-based cost ceilings may underestimate potential reliability benefits. Coating aging was also excluded from the 10-year analysis. In practice, dust accumulation, humidity, and weathering may alter solar-band optical losses and long-wave emissivity, affecting cooling performance over time. Given the small predicted benefit of radiative cooling alone, such changes could further reduce its economic viability. Accordingly, the reported cost ceilings for radiative and hybrid configurations should be viewed as optimistic screening-level upper bounds under the assumption of unchanged coating properties.

Table 10. Ten-year central economic case at 0.141 USD kWh^{-1}, 6% real discount rate, and 0.5% annual PV energy degradation

Case	First-year gain (kWh kWp^{-1})	10-year gross ceiling (USD kWp^{-1})
C_1 Fins	34.20	34.80
C_2 Radiative ideal	1.33	1.35
C_3 Hybrid ideal	35.30	35.92

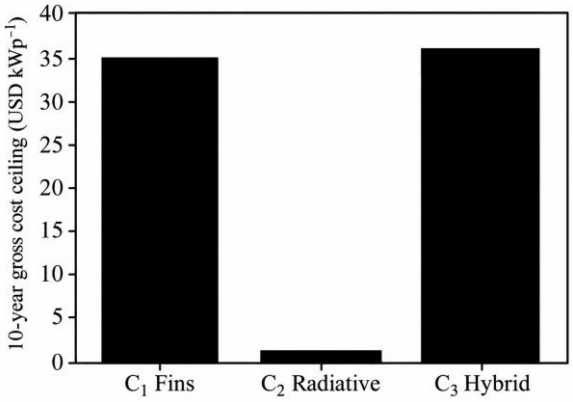


Figure 8. Ten-year gross installed-cost ceiling at the central electricity value

The modeled rear-fin cooling performance is qualitatively consistent with previous studies on passive PV heat sinks. Popovici et al. [14] reported temperature reductions using air-cooled heat sinks, while Bayrak et al. [15] highlighted the influence of fin geometry on cooling effectiveness. Hernandez-Perez et al. [16] investigated passive PV heat sinks through experimental and numerical analyses and subsequently examined discontinuous fin arrangements [17]. Dida et al. [18] reported experimental results under hot-arid conditions. However, these studies considered specific geometries and operating periods; therefore, their cooling results cannot be directly applied to the present annual assessment. Previous research also demonstrated the potential of radiative cooling under sunlight [19], its application to solar cells [20], possible PV efficiency improvements [21], and selective-spectral thermal management [22]. In the present model, increasing emissivity from 0.88 to 0.95 provided only limited cooling, while even small solar-band optical losses could offset the resulting electrical benefit.

This study provides preliminary recommendations for selecting suitable PV panel cooling methods in hot arid regions; however, generalizability to other facilities is unclear. Factors such as panel technology, orientation, building geometry, tilt angle, spacing at the back, air flow and local climatic conditions can affect the efficiency of cooling processes. Among various techniques evaluated, panels with rear fins were found to be more consistently effective in increasing annual energy production, when there was enough space for ventilation at the back of panels. Performance of high emissivity panels, however, greatly depended on optical losses and therefore such parameters as coating properties, dust contamination, sky view factor and thermal properties became very important. Using both technologies simultaneously led to small improvement in comparison with fins alone and therefore combined approach needs to be considered separately in every particular case. The thresholds for economic viability given in this paper are to be considered as indicative rather than real cost of installation due to dependence on local electric prices and financial conditions of the projects.

One of the main strengths of this work is its use of a full-year dataset to assess the proposed cooling strategies. Field measurements were used to characterize the reference PV module, while an 8,760-hour meteorological record allowed seasonal variations to be considered. Monthly heat-loss coefficients were applied to represent changes in thermal behavior throughout the year, and optical losses were included in the calculations. Each cooling configuration was also assessed against a consistently recalculated reference case. However, the experimental tests were confined to the reference module only, with the rear-finned, enhanced emissivity and hybrid designs analyzed by means of numerical simulation. Thus, any reduction in module temperature and increase in energy yield that have been reported can be seen as predicted values resulting from modeling and not validated experimentally. Indeed, factors such as the quality of fins' contact, thermal resistance, flow dynamics in three dimensions, wake effects, optical properties of coatings, soiling and aging, and installation conditions can affect the cooling performance. A further limitation comes from employing two Sandia data sets, namely, one for reference-module temperatures fit, which includes an incomplete record for January, and another for hourly weather conditions. Since downwelling longwave irradiance measurements were not available on an hourly basis, they were estimated, which can lead to errors. The results obtained pertain to only one location and year, while the normalized DC yields do not include all losses.

The results should not be used to generalize directly to other hot-arid environments, since the U_0 and U_1 parameters have been estimated for the particular module being studied, along with the way it is mounted and the local heat transfer environment. Using these parameters for another location would be an analysis of the sensitivity of the cooling to the new weather conditions and not an independent climatic verification. This would

require either a local thermal calibration or validation of the transferable model. It would also be useful to investigate multiple years and climatic zones for the validity of the cooling ranking system. The results presented here are particular to the type of PV module technology under consideration. The differences in glass backsheet and glass/glass modules will be reflected in the different rear surface emissivities, laminate thermal resistance and capacitance, and heat dissipation, which will result in different heat loss parameters and rear fin cooling performance.

Considering all the above constraints, the paper presents initial findings rather than an evaluation of commercially available cooling systems. The simulation results show that fins located at the back are more promising for further manufacturing and testing over the period of one year. Enhanced-emissivity cooling may also be considered where solar-band optical losses and coating costs are negligible.

4. Conclusions

This study used field-characterized reference-module data and annual meteorological records to evaluate rear-fin, enhanced-emissivity, and hybrid passive-cooling configurations through numerical modeling. Field measurements were available only for the reference module, while all cooling configurations were assessed numerically. Rear fins showed the most robust performance, reducing mean daylight module temperature by 2.54 °C, decreasing operating hours above 55 °C from 437 to 158 h, and increasing normalized annual DC yield by 34.20 kWh kWp^{-1} (1.56%). Radiative cooling alone provided an ideal gain of 0.061%, eliminated by a solar-band optical loss of 0.068%. The ideal hybrid achieved a 1.61% gain, only 1.10 kWh kWp^{-1} above fins alone. Under the central economic scenario, the 10-year gross installed-cost ceilings were 34.80 and 35.92 USD kWp^{-1} for fins and the ideal hybrid, respectively, leaving just 1.12 USD kWp^{-1} for the radiative component. Across the uncertainty samples, positive gains were predicted in 100% of fin cases, 99.9% of hybrid cases, and 6.1% of radiative cases.

The main limitation of this study is the lack of direct experimental testing of the proposed cooling configurations. Therefore, the predicted thermal improvements, energy gains, optical-loss thresholds, and economic limits remain model-based estimates requiring field validation. Future work should include year-long comparative testing of reference and cooled PV modules, considering mounting conditions, rear ventilation, sky exposure, and other site-specific factors.

Acknowledgements

The author thanks Sandia National Laboratories and the PV Performance Modeling Collaborative for releasing the field and annual performance datasets.

Nomenclature

A_f	Effective added fin surface area (m^2)
A_p	Reference Photovoltaic module area (m^2)
C_0	Reference Photovoltaic module case
C_1	Rear-fin cooling case
C_2	Enhanced-emissivity (radiative-cooling) case
C_3	Hybrid rear-fin and enhanced-emissivity case
C_{max}	Maximum allowable installed cost (USD kWp^{-1})
d	Annual degradation rate
ΔE	Annual incremental DC energy (kWh kWp^{-1})
ΔE_1	Incremental DC energy in the first year (kWh kWp^{-1})
ε	Long-wave emissivity
F_{sky}	Sky-view factor
G	Plane-of-array irradiance ($W\ m^{-2}$)
γ	Power-temperature coefficient (K^{-1})
h	Fin convective coefficient ($W\ m^{-2}\ K^{-1}$)
h_0	Intercept of the fin convection relation ($W\ m^{-2}\ K^{-1}$)
h_v	Wind-speed coefficient in fin convection relation ($W\ m^{-2}\ K^{-1}$ per $m\ s^{-1}$)
k	Thermal conductivity of the fin material ($W\ m^{-1}\ K^{-1}$)
L	Fin length (m)
L_c	Corrected fin length (m)
$L_\downarrow$	Downwelling long-wave irradiance ($W\ m^{-2}$)
ℓ	Solar-band optical-loss fraction
m	Straight-fin parameter (m^{-1})
N	Economic-analysis time horizon (years)
P_{DC}	DC output power (W)
P_{STC}	Rated power at standard test conditions (W)
P_e	Electricity price (USD kWh^{-1})
r	Discount rate

σ	Stefan-Boltzmann constant (W m^{-2} K^{-4})
t	Fin thickness (m)
T_a	Ambient air temperature (°C)
T_c	Photovoltaic cell temperature (°C)
T_m	Photovoltaic module-back temperature (°C)
U_0	Faiman zero-wind heat-loss coefficient (W m^{-2} K^{-1})
U_1	Faiman wind-dependent heat-loss coefficient (W m^{-2} K^{-1} per m s^{-1})
$U_{0,m}$	Month-specific zero-wind Faiman heat-loss coefficient (W m^{-2} K^{-1})
$U_{1,m}$	Month-specific wind-dependent Faiman heat-loss coefficient (W m^{-2} K^{-1} per m s^{-1})
U_{fin}	Additional effective fin heat-transfer conductance (W m^{-2} K^{-1})
υ	Wind speed (m s^{-1})
y	Year index in the economic calculation
η_c	Fin-to-module contact effectiveness
η_f	Straight-fin efficiency

References

[1] Jones, A. D., & Underwood, C. P. (2001). A thermal model for photovoltaic systems. *Solar Energy*. ***70***(4), 349–359. DOI: 10.1016/S0038-092X(00)00149-3

[2] King, D. L., Boyson, W. E., & Kratochvil, J. A. (2004). Photovoltaic Array Performance Model (SAND2004-3535). *Sandia National Laboratories*. DOI: 10.2172/919131

[3] Faiman, D. (2008). Assessing the outdoor operating temperature of photovoltaic modules. *Progress in Photovoltaics: Research and Applications*. ***16***(4), 307–315. DOI: 10.1002/pip.813

[4] Kaldellis, J. K., Kapsali, M., & Kavadias, K. A. (2014). Temperature and wind-speed impact on the efficiency of PV installations: Experience obtained from outdoor measurements in Greece. *Renewable Energy*. ***66***, 612–624. DOI: 10.1016/j.renene.2013.12.012

[5] Du, Y., et al. (2016). Evaluation of photovoltaic panel temperature in realistic scenarios. *Energy Conversion and Management*. ***108***, 60–67. DOI: 10.1016/j.enconman.2015.10.059

[6] Skoplaki, E., & Palyvos, J. A. (2009). On the temperature dependence of photovoltaic module electrical performance: A review of efficiency and power correlations. *Solar Energy*. ***83***(5), 614–624. DOI: 10.1016/j.solener.2008.10.008

[7] Driesse, A., Stein, J. S., & Theristis, M. (2022). Improving Common PV Module Temperature Models by Incorporating Radiative Losses to the Sky *Sandia National Laboratories*. DOI: 10.2172/1884890

[8] Han, J.-Y., Li, S.-Y., & Chen, Y.-C. (2025). Estimation of solar photovoltaic efficiency under the urban heat island effect. *Renewable Energy*. ***242***, 122492. DOI: 10.1016/j.renene.2025.122492

[9] Golzarroshan, S., et al. (2026). Unveiling the impact of Urban Heat Island (UHI) effect on photovoltaic panel efficiency: A case study in Mashhad, Iran. *Energy Reports*. ***15***, 109044. DOI: 10.1016/j.egyr.2026.109044

[10] Hoseinzadeh, P., et al. (2021). Energy performance of building integrated photovoltaic high-rise building: Case study, Tehran, Iran. *Energy and Buildings*. ***235***, 110707. DOI: 10.1016/j.enbuild.2020.110707

[11] Talaei, M., & Sangin, H. (2026). Comprehensive assessment of energy, daylight and visual comfort of rooftop and shading building-integrated photovoltaics across desert, steppe, and Mediterranean climates. *Advances in Building Energy Research*. ***20***(1), 62–103. DOI: 10.1080/17512549.2025.2562193

[12] Mustafa, R., et al. (2024). An innovative air-cooling system for efficiency improvement of retrofitted rooftop photovoltaic module using cross-flow fan. *International Journal of Renewable Energy Development*. ***13***(2), 223–234. DOI: 10.14710/ijred.2024.53077

[13] Cuce, E., Bali, T., & Sekucoglu, S. A. (2011). Effects of passive cooling on performance of silicon photovoltaic cells. *International Journal of Low-Carbon Technologies*. ***6***(4), 299–308. DOI: 10.1093/ijlct/ctr018

[14] Popovici, C. G., et al. (2016). Efficiency improvement of photovoltaic panels by using air-cooled heat sinks. *Energy Procedia*. ***85***, 425–432. DOI: 10.1016/j.egypro.2015.12.223

[15] Bayrak, F., Oztop, H. F., & Selimefendigil, F. (2019). Effects of different fin parameters on temperature and efficiency for cooling of photovoltaic panels under natural convection. *Solar Energy*. ***188***, 484–494. DOI: 10.1016/j.solener.2019.06.036

[16] Hernandez-Perez, J. G., et al. (2020). A new passive PV heatsink design to reduce efficiency losses: A computational and experimental evaluation. *Renewable Energy*. ***147***, 1209–1220. DOI: 10.1016/j.renene.2019.09.088

[17] Hernandez-Perez, J. G., et al. (2021). Thermal performance of a discontinuous finned heatsink profile for PV passive cooling. *Applied Thermal Engineering*. ***184***, 116238. DOI: 10.1016/j.applthermaleng.2020.116238

[18] Dida, M., et al. (2021). Experimental investigation of a passive cooling system for photovoltaic modules efficiency improvement in hot and arid regions. *Energy Conversion and Management*. ***243***, 114328. DOI: 10.1016/j.enconman.2021.114328

[19] Raman, A. P., et al. (2014). Passive radiative cooling below ambient air temperature under direct sunlight. *Nature*. ***515***, 540–544. DOI: 10.1038/nature13883

[20] Zhu, L., et al. (2014). Radiative cooling of solar cells. *Optica*. ***1***(1), 32–38. DOI: 10.1364/OPTICA.1.000032

[21] Safi, T. S., & Munday, J. N. (2015). Improving photovoltaic performance through radiative cooling in both terrestrial and extraterrestrial environments. *Optics Express*. ***23***(19), A1120–A1128. DOI: 10.1364/OE.23.0A1120

[22] Sun, X., et al. (2017). An optics-based approach to thermal management of photovoltaics: Selective-spectral and radiative cooling. *IEEE Journal of Photovoltaics*. ***7***(2), 566–574. DOI: 10.1109/JPHOTOV.2016.2646742

[23] Theristis, M., & Stein, J. S. (2023). PV Performance Modeling - Data and Resources [Data set]. *DuraMAT Data Hub*. DOI: 10.21948/1970772

[24] Driesse, A., Theristis, M., & Stein, J. S. (2023). PV Module Operating Temperature-Data and Resources [Data set]. *DuraMAT Data Hub*. DOI: 10.21948/2204673

[25] Driesse, A., Theristis, M., & Stein, J. S. (2023). PV module operating conditions and temperature measurements: an open dataset for PV research *Sandia National Laboratories*. DOI: 10.2172/2293574

[26] Holmgren, W. F., Hansen, C. W., & Mikofski, M. A. (2018). pvlib python: a Python package for modeling solar energy systems. *Journal of Open Source Software*. ***3***(29), 884. DOI: 10.21105/joss.00884

[27] Anderson, K. S., et al. (2023). pvlib python: 2023 project update. *Journal of Open Source Software*. ***8***(92), 5994. DOI: 10.21105/joss.05994

[28] Swinbank, W. C. (1963). Long-wave radiation from clear skies. *Quarterly Journal of the Royal Meteorological Society*. ***89***(381), 339–348. DOI: 10.1002/qj.49708938105

[29] Palyvos, J. A. (2008). A survey of wind convection coefficient correlations for building envelope energy systems' modeling. *Applied Thermal Engineering*. ***28***, 801–808. DOI: 10.1016/j.applthermaleng.2007.12.005

[30] Dobos, A. P. (2014). PVWatts Version 5 Manual *National Renewable Energy Laboratory*. DOI: 10.2172/1158421

[31] McKay, M. D., Beckman, R. J., & Conover, W. J. (1979). A comparison of three methods for selecting values of input variables in the analysis of output from a computer code. *Technometrics*. ***21***(2), 239–245. DOI: 10.1080/00401706.1979.10489755

[32] Feldman, D., et al. (2021). U.S. Solar Photovoltaic System and Energy Storage Cost Benchmark: Q1 2020 *National Renewable Energy Laboratory*. DOI: 10.2172/1764908

[33] Jordan, D. C., & Kurtz, S. R. (2013). Photovoltaic degradation rates—an analytical review. *Progress in Photovoltaics: Research and Applications*. ***21***(1), 12–29. DOI: 10.1002/pip.1182

[34] Huang, M., et al. (2025). Quantifying the effects of dust characteristics on the performance of radiative cooling PV systems. *Applied Energy*. ***377***, 124672. DOI: 10.1016/j.apenergy.2024.124672

[35] Hossain, M. I., et al. (2022). Anti-Soiling Coatings for Enhancement of PV Panel Performance in Desert Environment: A Critical Review and Market Overview. *Materials*. ***15***(20), 7139. DOI: 10.3390/ma15207139